Progress In Electromagnetics Research C, Vol. 101, 219–232, 2020

Analysis and Optimization of Double-Side Hybrid Excitation Flux-Switching Motor

Yunyun Chen[1, *], Tongle Cai[1], Jiahong Zhuang[1], and Xiaoyong Zhu[2]

Abstract—In this paper, a double-side hybrid excitation flux-switching (DSHE-FS) motor employing a double stator structure with special multi-excitations is presented. The high space utilization improves the torque density and power density of DSHE-FS motor. The addition of non-rare-earth permanent magnet material reduces the consumption of rare-earth permanent magnet material. The double-side field windings enable the motor to have more flexible magnetic modulation properties. To investigate the principle of motor operation and flux regulation, the equivalent magnetic circuit method is employed. In order to achieve higher operation performances of the motor in different driving modes, the multi-objective optimization with coupled multi-physical field calculation is carried out. The multi-physical comprehensive sensitivity function is defined which couples the electromagnetic performance optimization objective and mechanical performance objective. Then multi-objective genetic algorithm (MOGA) method was used to find a feasible solution set. Response surface (RS) method and parameter scan method are used to further determine the five important dimensions. The electromagnetic characteristics of optimized DSHE-FS motor are evaluated and compared in detail. Moreover, the mechanical analysis is conducted for the cupped rotor of DSHE-FS motor to validate the operation security. Theoretical analysis and simulation results verify the rationality of the DSHE-FS motor and the proposed optimization design method.

1. INTRODUCTION

Recently, the rapid development of green electric vehicles (EVs) has promoted the design optimization researches of different types of electrical machines. Since the driving environments faced by EVs are complex, the advanced qualities of high power density, high efficiency over wide speed range, and high reliability are often required during the design of EV motors [1, 2]. Among them, flux-switching permanent magnet (FSPM) machines have been widely investigated due to the advantages of robust rotor structure, low torque ripple, and high efficiency [3, 4]. And yet, the unstable supply and sharp price fluctuation of rare earth permanent magnet materials may directly affect the cost of FSPM motors, where the consumption of rare-earth permanent magnet material is usually large. So, how to improve the utilization of rare-earth permanent magnet and reduce the amount of rare-earth permanent magnet material may become one of the new research contents of FSPM motor design [5]. Replacing rare-earth permanent magnet with non-rare-earth ferrite is undoubtedly the most direct way to reduce the consumption of rare-earth permanent magnet materials for such FSPM motors [6, 7]. Yet, due to the low remanence of the non-rare-earth ferrite, in order to ensure the torque output of the motor, a larger size of the non-rare earth ferrite is required, often several times of the size of the rare-earth permanent magnet material. Nevertheless, in the conventional FSPM motor, since both armature windings and permanent magnets are placed in the stator, the stator space is often limited, and it is difficult to place

Received 14 March 2020, Accepted 26 April 2020, Scheduled 11 May 2020
* Corresponding author: Yunyun Chen (yychen@yzu.edu.cn).
[1] College of Electrical, Energy and Power Engineering, Yangzhou University, Yangzhou 225009, China. [2] School of Electrical and Information Engineering, Jiangsu University, Zhenjiang 212013, China.

a large volume of non-rare earth ferrite. On the one hand, such a complex stator structure restricts the numbers of PMs and armature windings, thus limiting the improvements of the electromagnetic performance. On the other hand, it is not conducive to the improvement of heat dissipation ability [8].

Recently, a new type of partitioned stator flux-switching permanent magnet motor with two separated stators is presented and analyzed in [9]. In such a partitioned stator FSPM motor, the PMs and armature windings are placed in the outer stator and inner stator, separately, which can relieve the severe space competition and enhance motor efficiency and torque density. Nevertheless, in terms of flux regulating performance, such kind of motor is still similar to a traditional permanent magnet motor. It is difficult to regulate the air gap magnetic field of the motor, which leads to the fixed constant power operation region and a narrow speed range [10].

In this paper, by integrating a new concept of partitioned-stator and multi-excitation into a flux switching motor, a double-side hybrid excitation flux-switching (DSHE-FS) motor is proposed and investigated. In the proposed DSHE-FS motor, the hybrid-PMs of rare-earth NdFeB and non-rare-earth ferrite are applied to reduce the consumption of rare-earth PM material while keeping high torque density. Moreover, with inner and outer field windings equipped in the outer and inner stators separately, more flexible flux adjustment can be achieved, and more wide speed range can be obtained effectively. The paper is organized as follows. The topology of the DSHE-FS motor is given, and the basic operation and principle of magnetic flux modulation are illustrated by using the equivalent magnetic circuit method. Then, in Section 3, the multi-objective optimization with coupled multi-physical field calculation is newly carried out. The electromagnetic characteristics of optimized DSHE-FS motor are evaluated and compared in detail in Section 4. Moreover, the mechanical analysis is conducted for the cupped rotor of DSHE-FS motor to validate the operation security. The performance comparison between the initial and the optimized motor verifies the optimization of DSHE-FS motor. Finally, some conclusions are drawn in Section 5.

2. MOTOR STRUCTURE AND OPERATING PRINCIPLE

In order to highlight the structural characteristics of the proposed DSHE-FS motor, in Figure 1, the structure of the proposed motor and the structure of a conventional hybrid excitation flux switching motor (HEFSM) are presented. It can be seen that the DSHE-FS motor makes full use of the internal space of the motor, and the structure is more complex than the conventional HEFSM. From Figure 1(b), the armature windings and hybrid PMs are placed in outer and inner stators separately to alleviate the spatial conflicts in the limited stator of conventional FSPM motor. In the outer stator, the wide armature teeth and narrow field excitation teeth are evenly distributed around the circumference and are staggered along the radial direction. In the inner stator, rare-earth NdFeB-PMs and non-rare-earth ferrite-PMs are arranged in parallel, which can effectively reduce the coupling interference of hybrid PMs. The field windings around ferrite-PMs can act as supplementary electric excitation windings. It

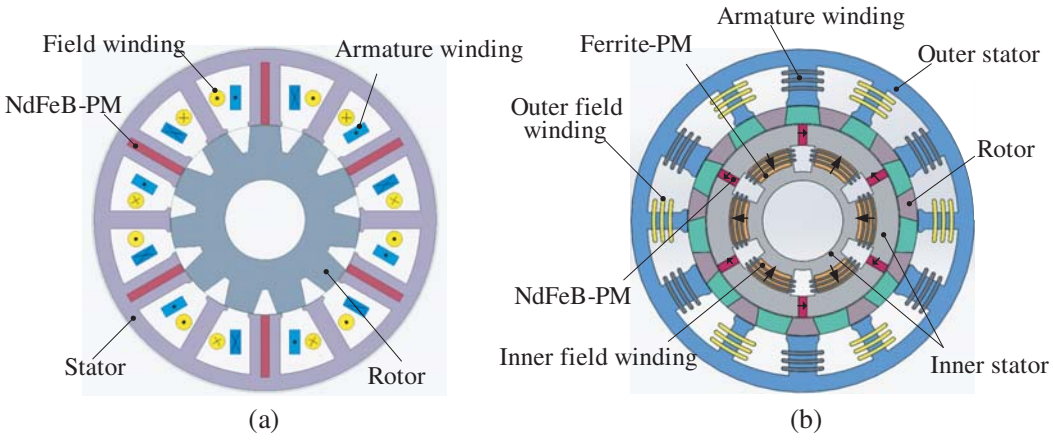

Figure 1. Structure of motors. (a) Conventional HEFSM. (b) Proposed DSHE-FS motor.

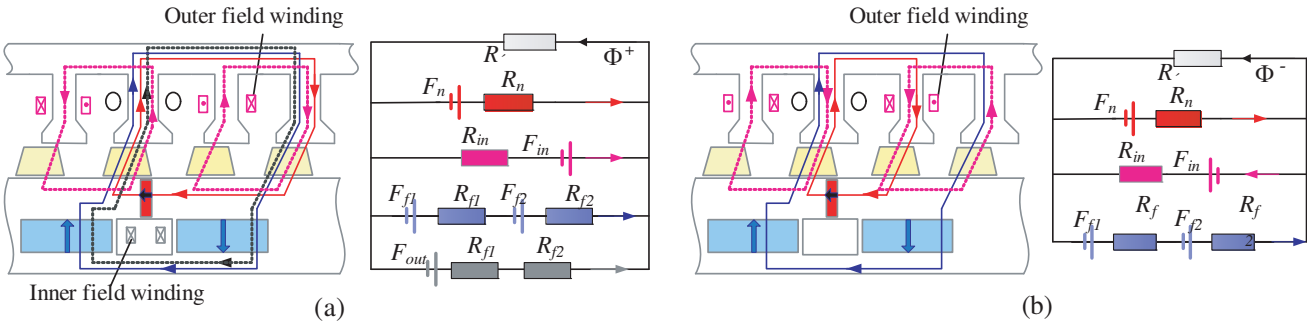

Figure 2. Principle of magnetic flux regulation of the DSHE-FS motor. (a) Flux-enhancement mode. (b) Flux-weakening mode.

is noted that the double-side inner and outer field windings make the field adjustment more flexible and can avoid the potential risk of non-rare-earth ferrite-PMs demagnetization.

Figure 2 shows the principle of magnetic flux regulation at different operation modes of flux enhancement and flux weakening [11, 12]. From the figure, the magnetic flux path and corresponding equivalent magnetic circuit are illustrated. In the figure, R_n, R_{f1}, R_{f2}, and R_δ are magnetic reluctance of NdFeB-PM, two ferrite-PMs, and air-gap, respectively. F_{out}, F_{in}, F_n, and F_f are magnetomotive forces (MMFs) of double-side inner and outer field windings and PMs, respectively. Φ^+ and Φ^- are the air-gap flux amplitudes under flux-enhancement and flux-weakening, respectively.

At the flux-enhancement mode, from Figure 2(a), when the positive currents are both applied in double-side field windings, the flux lines enter the outer stator teeth and join the PM flux in the same direction, and consequently enhance the motor main flux. On the other hand, at the flux-weakening mode, in Figure 2(b), in order to prevent demagnetization of ferrite PM resulting from negative current, only negative inner field current is employed in flux-weakening condition. The flux is maintained, but the direction is reversed to weaken the main flux path. Thus the flux density can be regulated flexibly, and the speed range can be further widened.

Then, Figure 3 shows the magnetic field distributions and flux linkage waveforms with different excitations conditions [13]. It can be seen that when double-side inner and outer field windings work together with the current density varying from 0 to 20 A/mm^2, the amplitude of flux linkage increases from 0.07 Wb to 0.12 Wb, which widens the range of flux regulation.

Here, to clarify the capability of flux regulation, a flux regulation ratio δ is defined as follows to evaluate the validity of field windings:

$$\delta = \frac{\Phi\left(\pm i_{fout}, +i_{fin}\right)}{\Phi_{PM}} \tag{1}$$

As illustrated in Figure 2, Φ is the flux amplitude with different outer field currents $\pm i_{fout}$ and inner field currents $+i_{fin}$ under flux-enhancement mode and flux-weakening mode, respectively. Φ_{PM} is the flux amplitude excited by hybrid PMs only. The higher δ indicates a better flux regulation capability. Due to the double-side inner and outer field windings, the magnetic field adjustment of the DSHE-FS motor is more flexible.

3. MULTI-OBJECTIVE OPTIMAL DESIGN

3.1. Multiple Design Requirements

Considering the potential application prospect of DSHE-FS motor in EVs, the proposed DSHE-FS motor should offer multiple driving modes in the early stage of motor design according to the requirements at different EV driving cycles [14, 15]. For example, the flux-enhancement mode with high torque output is preferred to meet the frequent start, acceleration, or overloaded climbing. Then the flux-weakening mode with high flux regulation ratio is often necessary to realize the high-speed cruise. Thus the multiple driving modes and multi-optimization target make the optimal design of the DSHE-FS motor

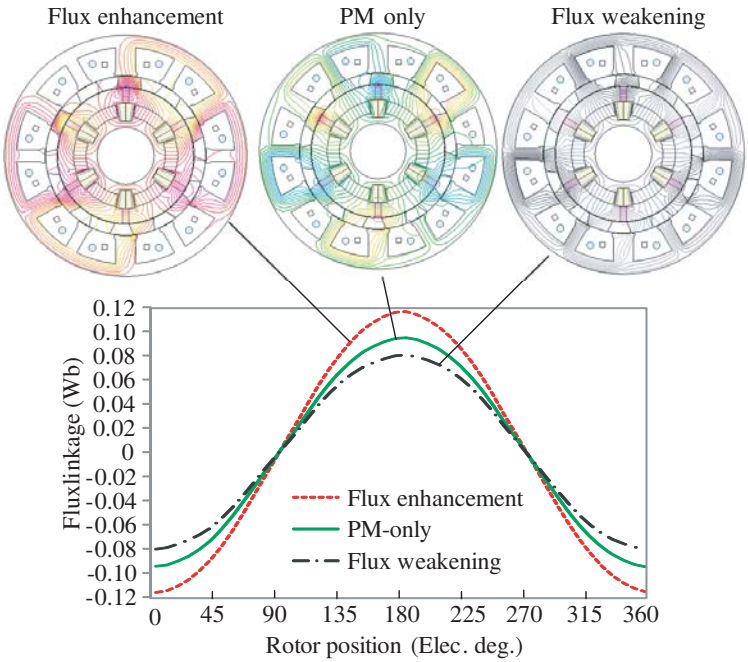

Figure 3. Magnetic field distribution and flux linkages under the different excitations.

flexible and complicated [16]. In addition, as the cupped rotor with a large radius and double air-gap is employed, the DSHE-FS motor suffers from high centrifugal force and mechanical stress [17, 18].

Based on the above considerations, in the optimization design process of DSHE-FS MOTOR, it is also necessary to add the equivalent stress and deformation into the optimization objective, so as to realize the electromagnetic & mechanical coupling optimization design of the motor [19, 20]. The specific design process is shown in Figure 4. Here, ANSYS® software and MATLAB® software are used for simulation and optimization purpose.

3.2. Multiphysics Sensitivity Analysis

In this paper, the multi-physics comprehensive sensitivity analysis is newly utilized to investigate the various size parameters. Some electromagnetic performances, as well as mechanical performance, are selected to be optimization targets [21]. Thus, the comprehensive sensitivity function F_C, which includes five optimization objectives, i.e., torque ripple F_{Trip}, average torque F_T, flux regulation ratio F_δ, equivalent stress F_S, and deformation F_D, are defined as

$$F_C = \lambda_1 F_T + \lambda_2 F_{Trip} + \lambda_3 F_\delta + \lambda_4 F_S + \lambda_5 F_D \tag{2}$$

where $\lambda_1 \sim \lambda_5$ are the weight coefficients of five design objectives. Here $F_{Trip=}(T_{\max} - T_{\text{mean}})/T_{\text{mean}}$.

Considering that the size of permanent magnet is a direct influence factor on the cost of motor, the size of PM was firstly determined before design, and the initial design parameters are listed in Table 1.

Then sensitivity calculation and determination was carried out for all other design variables. The specific design variables and their value range are listed in Table 2, and the established parameterized model is shown in Figure 5.

Figure 6 exhibits the multi-physics comprehensive sensitivity analysis results. Here the positive and negative numbers indicate the positive and negative correlations. Through the comprehensive comparison of the eight parameters, it can be concluded that four key parameters including the arc of armature tooth *arc_s1*, the inner arc of rotor *arc_r2*, the armature tooth width h_b, and the guide bridge width b_r are the four main parameters that affect the electromagnetic performance. For the mechanical properties, h_b, b_r, and outer field tooth width h_s are sensitive parameters that need further optimization.

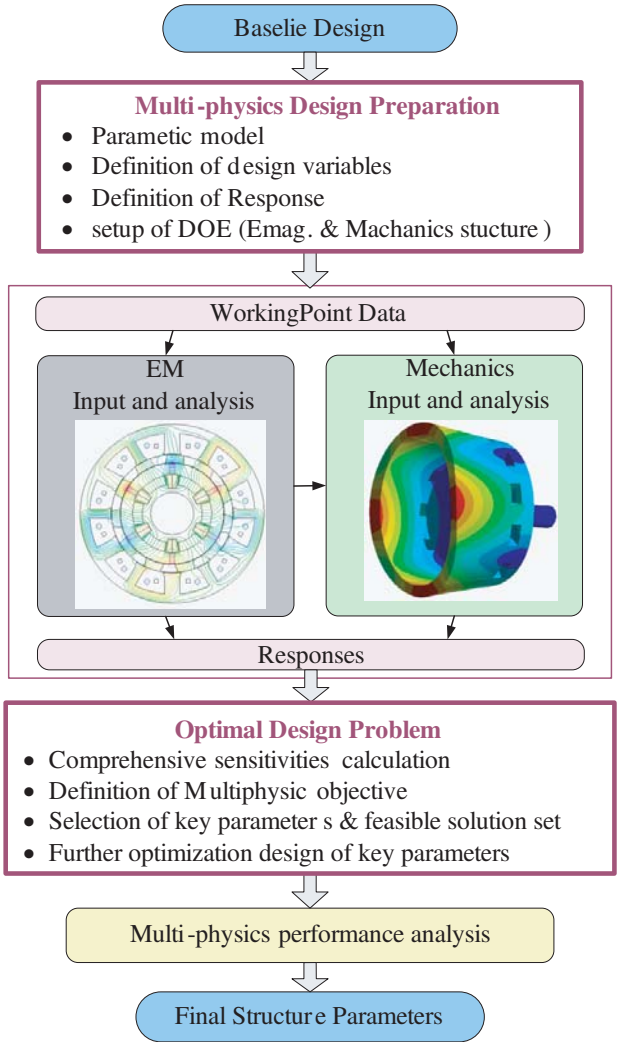

Figure 4. Multi-physics optimal design process of DSHE-FS motor.

Table 1. Initial design parameters.

Dimensions parameters	Size	Dimensions parameters	Size
Outer stator outer diameter	196 mm	Inner stator outer diameter	110 mm
Outer stator yoke height	10 mm	NdFeB PM height	12 mm
Arc of armature tooth	16°	NdFeB PM Mag. thick	5°
Arc of outer field tooth	10°	ferrite PM Mag. thick	10 mm
Armature tooth width	8 mm	ferrite PM width	30°
Outer field tooth width	5 mm	Inner air gap	0.7 mm
Middle rotor outer diameter	129 mm	Outer air gap	0.7 mm
Middle rotor yoke height	9 mm	Axle diameter	46 mm
Outer arc of rotor	16°	Axle length	70 mm
inner arc of rotor	21°		

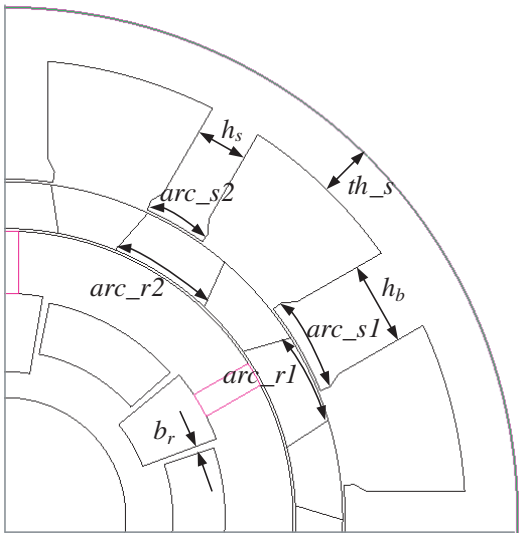

Figure 5. The parameterized model of DSHE-FS motor.

Table 2. Key design variables.

No.	Parameter	Design variables	Variation range
P1	*arc_s1*	Arc of armature tooth	14 deg ∼ 18 deg
P2	*arc_s2*	Arc of outer field tooth	10 deg ∼ 12 deg
P3	h_b	Armature tooth width	6 mm ∼ 12 mm
P4	h_s	Outer field tooth width	3 mm ∼ 6 mm
P5	*arc_r1*	Outer arc of rotor	14 deg ∼ 17 deg
P6	*arc_r2*	inner arc of rotor	18 deg ∼ 22 deg
P7	*th_s*	Thick of stator yoke	8 mm ∼ 14 mm
P8	b_r	Guide bridge width	1 deg ∼ 3.5 deg

As shown in Figure 7 and Figure 8, considering the coupling relationships among these eight design variables and between each variable and each optimization objective, the multi-objective genetic algorithm (MOGA) method in this paper is utilized to get the feasible solution set [22].

3.3. Comprehensive Optimization of Key Parameters

Through the multi-physical comprehensive sensitivity analysis above, five key sensitive parameters for the multi-optimization objective have been screened, and the feasible solution set has been obtained by using MOGA method. In this section, considering different operating conditions of the motor, five sensitive parameters will be further optimized by the way of scanning optimization and response surface [23]. According to the requirements under different driving modes, the optimization objectives of the DSHE-FS motor with flux-enhances and flux-weakening are also different. In the flux-enhanced driving mode for frequent start or climbing, the average torque and torque ripple can be selected as the optimization objectives. In the flux-weakening driving mode for high speed cruise, the core loss and flux regulation ratio δ are chosen to be the objectives. In addition, under high speed operation, the centrifugal force of the rotor increases obviously, so the structural stress and total deformation also need to be selected as optimization objectives.

Figure 9 depicts the response surface of average torque and torque ripple versus four key parameters h_b, b_r, *arc_r2*, and *arc_s1* generated by RS method. It can be seen that h_b and b_r do have a great influence

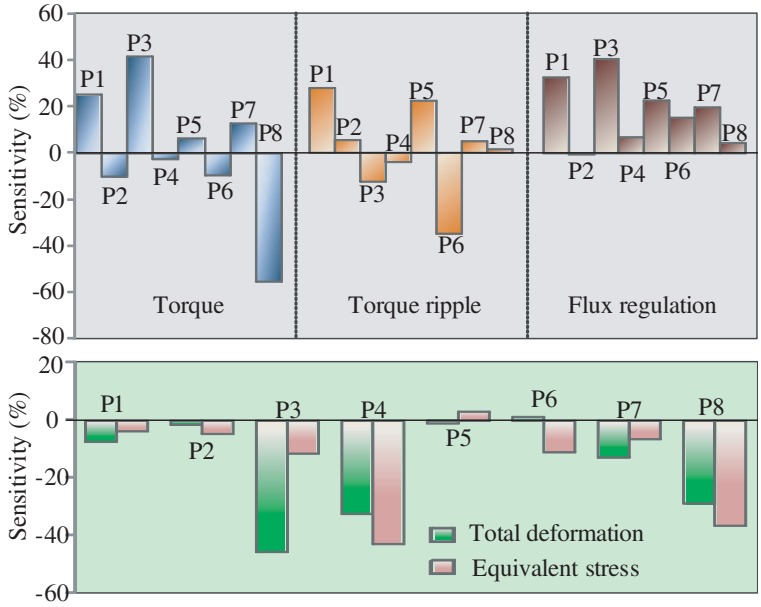

Figure 6. Multi-physics sensitivity analysis of DSHE-FS motor.

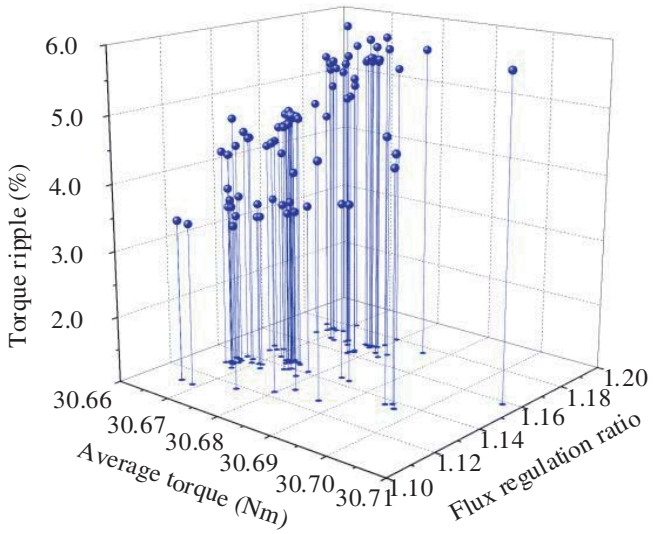

Figure 7. The electromagnetic optimization using MOGA method.

on the average torque, and the amplitude can vary from 24 Nm to 30 Nm. Similarly, *arc_r2* and *arc_s1* also have more influence on the torque ripple. After optimization, the torque ripple can be reduced by nearly half. Figure 10 shows the effects of two key parameters, in which the flux regulation ratio and core loss are both illustrated. As can be seen, the flux regulation ratio and core loss increase more significantly with increasing *arc_s1* and h_b, while the motor efficiency is sacrificed. For the three parameters h_b, h_s, and b_r that have great influence on the deformation and stress of the motor, RS optimization results are given in Figure 11. It can be seen that compared with the maximum value of deformation, the equivalent stress is more nonlinear with the change of key parameters b_r, h_s, and h_b.

Through further comprehensive comparison and analysis above, the optimum values of four key design parameters are determined and listed in Table 3.

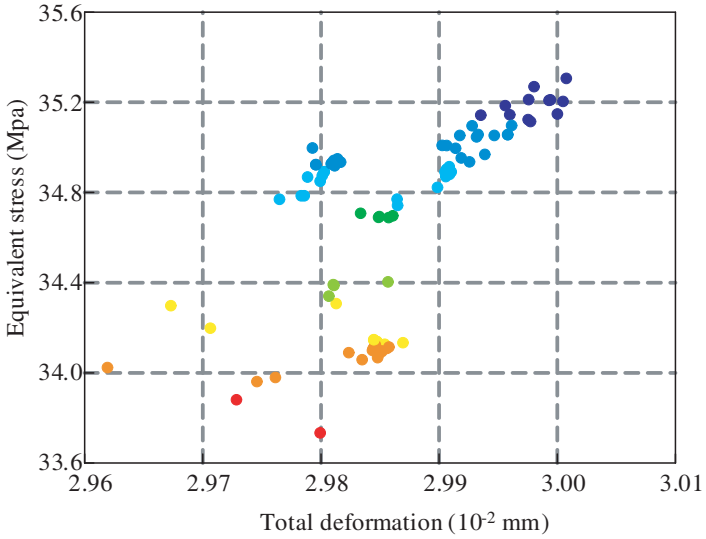

Figure 8. The mechanical structure optimization using MOGA method.

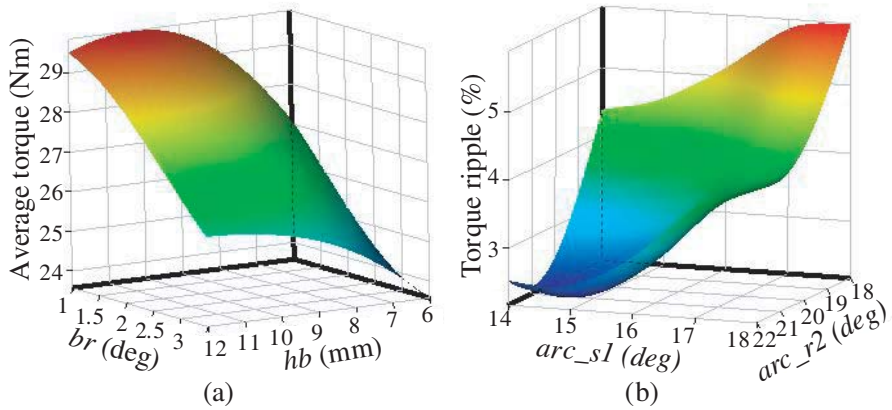

Figure 9. RS optimization of average torque and torque ripple in flux-enhanced driving mode. (a) Torque versus b_r and h_b. (b) Torque ripple versus *arc_s1* and *arc_r2*.

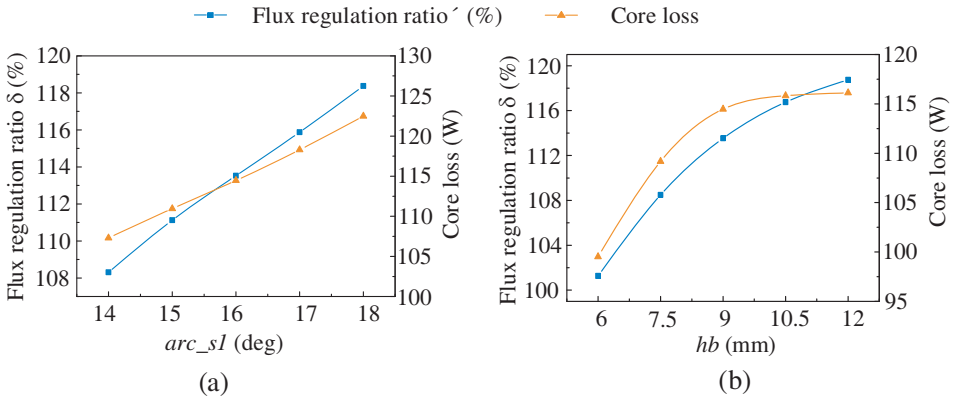

Figure 10. Variations of flux regulation ratio and core loss with different parameters in flux-weakening driving mode. (a) With *arc_s1* (b) with h_b.

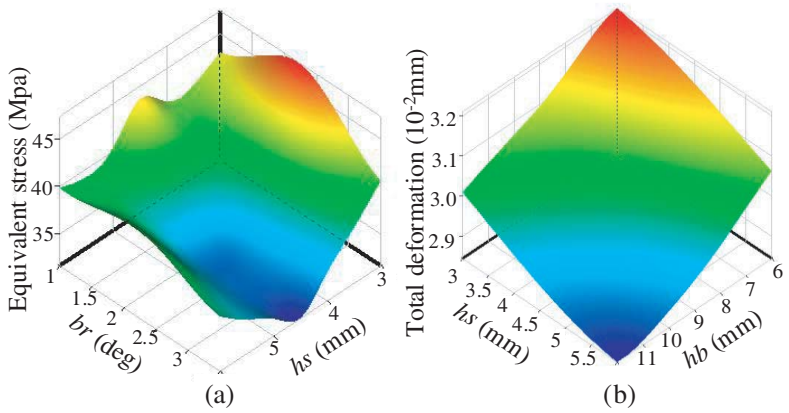

Figure 11. RS optimization of stress and deformation in high speed cruise driving mode. (a) Equiv stress *versus* b_r and h_s. (b) Total deformation versus h_s *and* h_b.

Table 3. Optimized key design parameters.

Parameter	Original	Optimized
Arc of armature tooth *arc_s1*	16 deg	17 deg
Arc of inner arc of rotor *arc_r2*	21 deg	19.5 deg
Armature tooth width *hb*	8 mm	10.5 mm
Guide bridge width *br*	2 deg	1 deg
Outer field tooth width *hs*	5 mm	4.5 mm

4. PERFORMANCE ANALYSIS

4.1. Back-EMF

The optimized DSHE-FS motor is obtained and compared with the initial design. As shown in Figure 12, the amplitude of no-load back EMF increases, and the waveform is more sinusoidal after optimization. Meanwhile, the harmonic contents decrease, and the amplitude of base wave increase obviously.

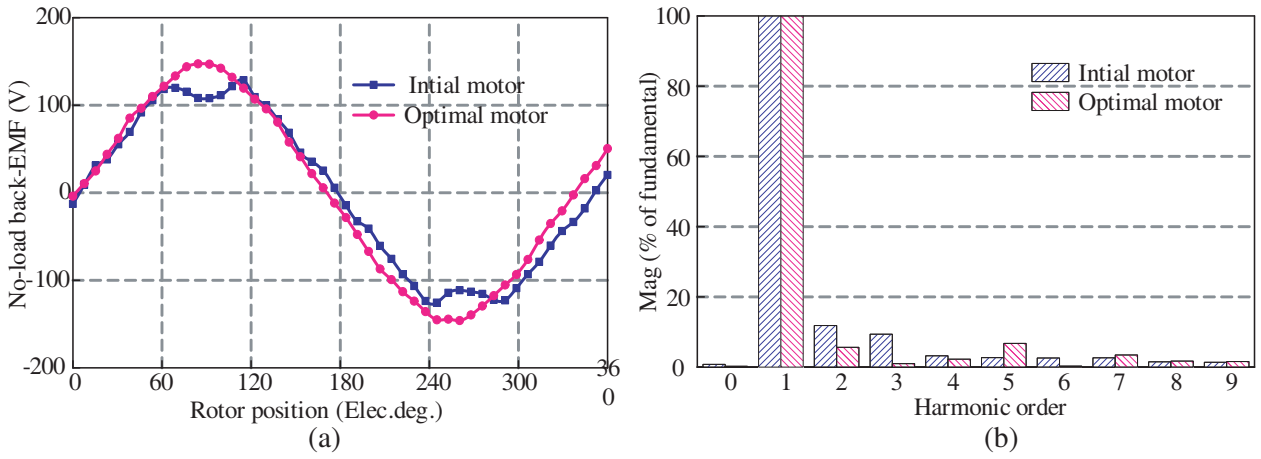

Figure 12. No-load back EMF comparison: (a) back EMF waveforms; (b) back EMF harmonic spectra.

4.2. Performance of Flux Regulation

Figure 13 shows the regulation results of different inner and outer excitation currents on no-load flux linkage, as well as the variation curve of corresponding flux regulation ratio δ. As shown in Figure 13(a), the flux regulation ratio δ decreases to 80% when -20 A is applied in outer field windings under the flux-weakening condition. When 20 A is applied to enhance the flux, δ reaches 125%. It can be seen that the flux regulation capability increases linearly with the outer excitation current. Considering the risk of irreversible demagnetization of ferrite PMs, for the inner field windings, only the flux enhancing performance is analyzed. As shown in Figure 13(b), the flux regulation ratio δ can be nearly 107% when 20 A is applied. The above analysis proves that when double-side inner and outer field windings work together, the range of flux regulation can be wider.

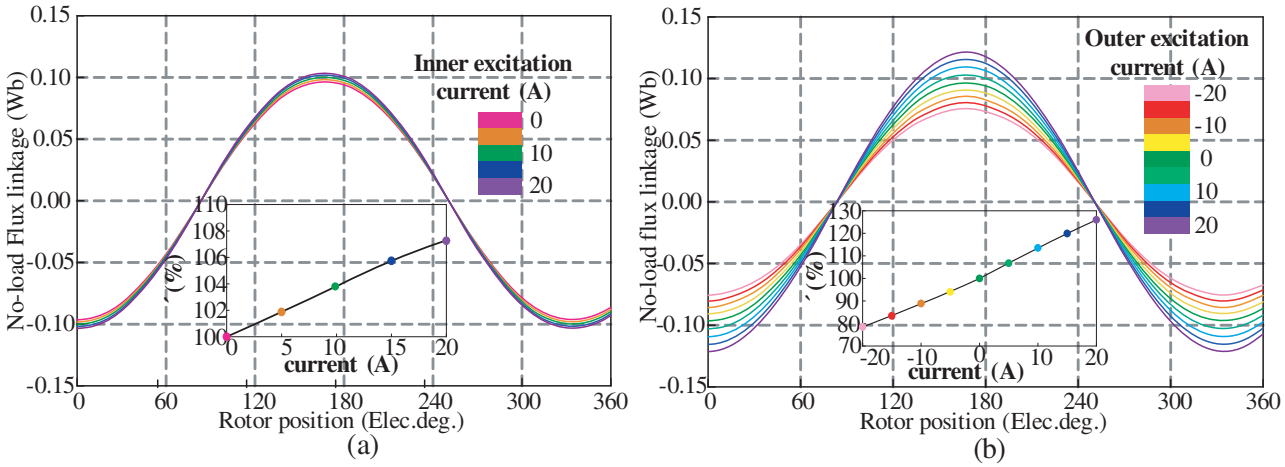

Figure 13. Flux regulation performance (a) of inner field excitation. (b) of outer field excitation.

4.3. Torque Capability

For rated operation driving mode, the static output torque comparison waveforms at rated load and cogging torque comparison waveforms at no load are shown in Figure 14. Obviously, the average output torque is enhanced from 26.2 Nm to 27.8 Nm while the torque ripple is reduced from 5.6% to 4.1%. Figure 15 gives the surface diagram of the rated average torque with different currents of the double-

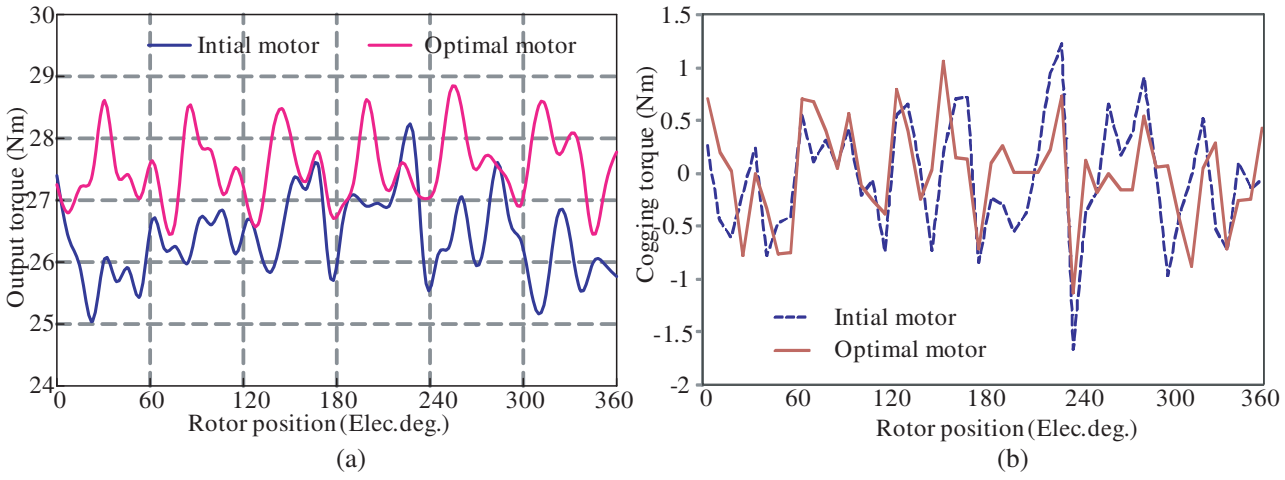

Figure 14. Torque capability. (a) static torque output (b) cogging torque.

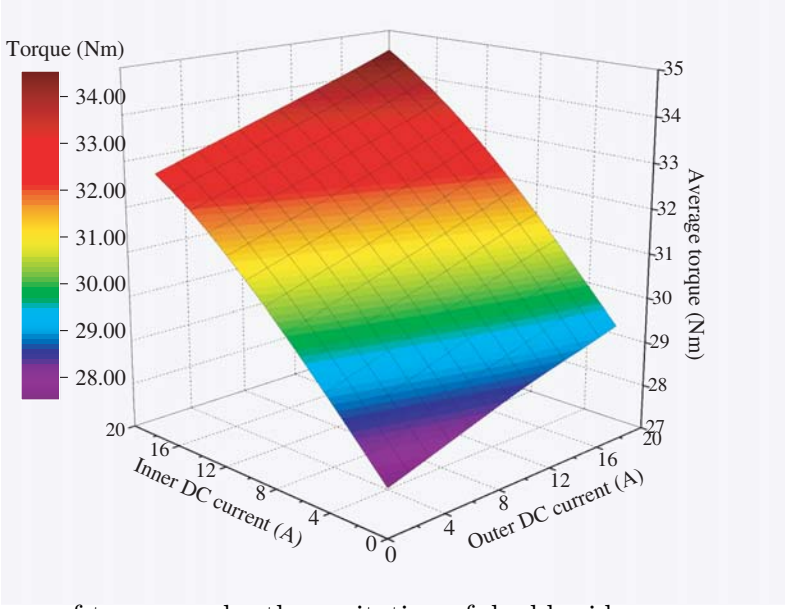

Figure 15. The change of torque under the excitation of double-side.

side inner and outer field windings. It can be seen that with the increase of current density of the double-side field windings, the output average torque is also increased. Compared with the inner field winding, the outer field winding has more obvious regulating effects on the average torque. All above results validate the previous analysis and prove the effectiveness of parameter optimization on advancing motor performance.

4.4. Operating Performance

Figure 16 shows the torque-speed characteristics corresponding to the global operation. It can be seen that in the constant torque region below the base speed, the output torque of the optimized motor is improved, and the speed range is also widened.

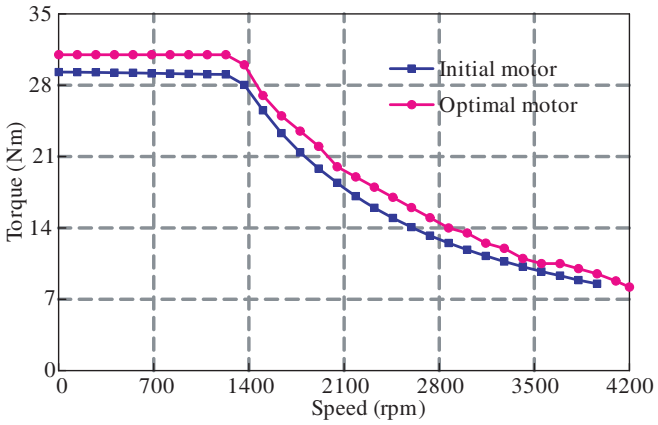

Figure 16. Torque-speed envelops.

4.5. Capability of Anti-Demagnetization

To analyze the capability of anti-demagnetization of the ferrite-PMs in the DSHE-FS motor, the q-axis current is chosen as 30 A which is twice that of the rated one [24]. Figure 17(a) gives the field distributions of the ferrite-PM. Considering that the knee value of the ferrite de-magnetization curve is

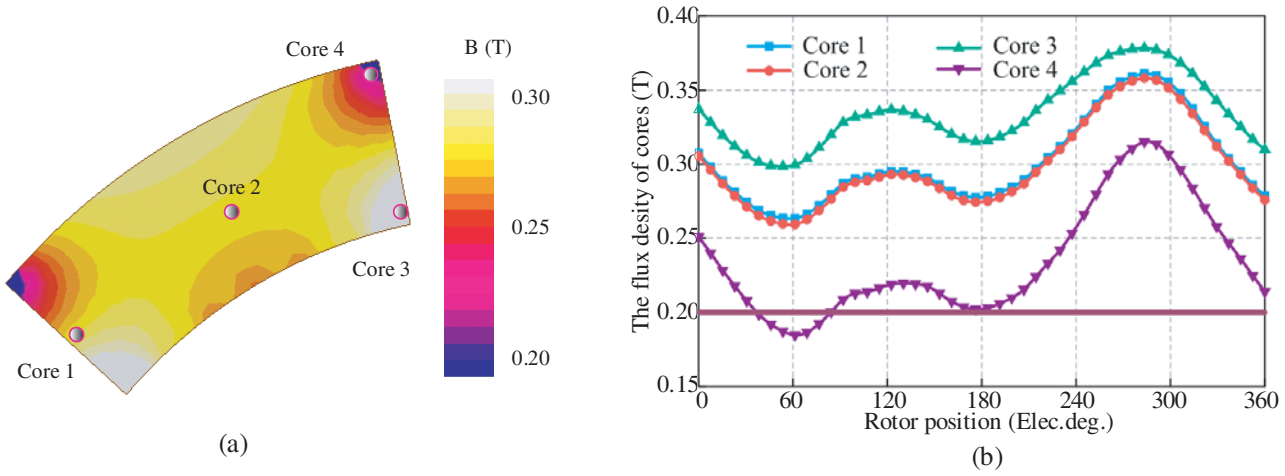

Figure 17. (a) Field distribution of the ferrite-PM. (b) Variations of flux densities at four typical points in the ferrite-PM.

about 0.2 T, it is defined that when the working point is lower than 0.2 T, the demagnetization of ferrite occurs. It can be seen that the demagnetization area is small. As shown in Figure 17(b), with inner field excitation, the magnetic flux densities only at point 4 will fall below 0.2 T. And the magnetic flux densities of other three different points are always higher than 0.2 T. It indicates that the DSHE-FS motor possesses high anti-demagnetization capabilities under the flux-weakening high-speed operation condition.

4.6. Mechanical Characteristic

As the cupped rotor with a large radius is employed, the DSHE-FS motor suffers from high centrifugal force and mechanical stress [25]. Thus it is important to carry out further analysis of mechanical characteristic to appraise the motor structure design. The cupped rotor consists of rotor pieces and is supported by fixed ring. The equivalent stress and total deformation of the rotor in the DSHE-FS motor are shown in Figure 18. The maximum stress occurring on the fixed ring is around 36 MPa. All stresses on the rotor are much smaller than the stress limits of rotor materials, which indicate that the rotor can operate securely. In addition, it can be seen that the farther away the rotor is from the end plate, the severer the deformation is. The maximum deformation of the rotor is 0.033 mm.

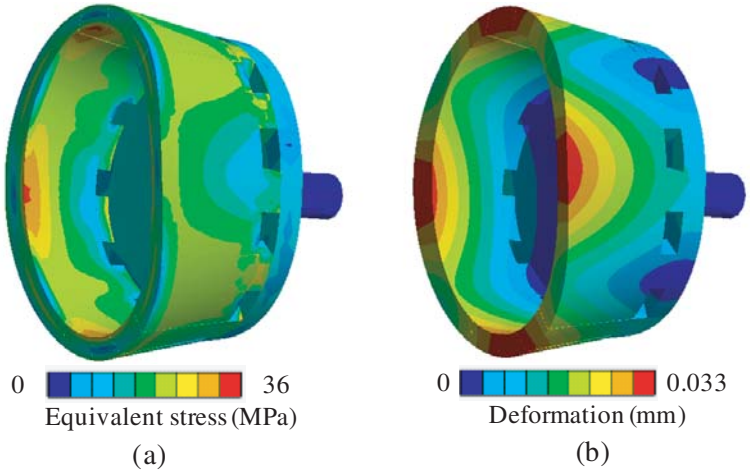

Figure 18. The mechanical analysis of DSHE-FS motor. (a) Equivalent stress (b) Deformation.

Table 4. Optimized comparison results.

Performance	Initial scheme	Optimal design
D-axis inductance	13.88 mH	15.64 mH
Q-axis inductance	14.32 mH	16.27 mH
Efficiency	88.21%	90.97%
Flux regulation ratio δ	15.08	23.32
Power factor	0.53	0.64

In addition, for the motor before and after optimization, the comparison results of inductance characteristics, efficiency, power factor, and flux regulation ratio are listed in Table 4.

5. CONCLUSIONS

In this paper, the DSHE-FS motor employing partitioned stators to accommodate armature windings, and multi-excitations are proposed. To meet the different requirements of motor in different driving modes, a multi-objective optimization design method with multi-physical field coupling calculation is proposed. Sensitivity analysis of size parameters is carried out, and the key size parameters are optimized by different optimization algorithms. The electromagnetic characteristics such as flux regulation capability and demagnetizing withstand capability of ferrite are investigated in detail. Further mechanical analysis is conducted for the cupped rotor of the DSHE-FS motor to validate the motor operation security. The comparison results also confirm the rationality of the structure and optimal design of the DSHE-FS motor.

ACKNOWLEDGMENT

This work was funded by the National Natural Science Foundation of China (Grant No. 51507151), and the Natural Science Foundation of the Jiangsu (Grant No. BK20150454).

REFERENCES

1. Hua, W., H. Zhang, M. Cheng, J. Meng, and C. Hou, "An outer-rotor flux-switching permanent-magnet-machine with wedge-shaped magnets for in-wheel light traction," *IEEE Trans. Ind. Electro.*, Vol. 64, No. 1, 69–80, 2017.
2. Lee Christopher, H. T., K. T. Chau, and C. Liu, "Electromagnetic design and analysis of magnetless double-rotor dual-mode machines," *Progress In Electromagnetics Research*, Vol. 142, 333–351, 2013.
3. Zhu, X., Z. Shu, L. Quan, Z. Xiang, and X. Pan, "Design and multi-condition comparison of two outer-rotor flux-switching permanent magnet motors for in-wheel traction applications," *IEEE Trans. Ind. Electron.*, Vol. 64, No. 8, 6137–6148, 2017.
4. Chen, Y., Y. Ding, X. Li, and X. Zhu. "Design and analysis of less-rare-earth double-stator modulated machine considering multi-operation conditions," *IEEE Trans. Appli. Supercond.*, Vol. 28, No. 3. Art. No. 5201405, 2018.
5. Sun, X., Y. Shen, S. Wang, et al., "Core losses analysis of a novel 16/10 segmented rotor switched reluctance BSG motor for HEVs using nonlinear lumped parameter equivalent circuit model," *IEEE/ASME Trans. Mechatro*, Vol. 23, No. 2, 747–757, 2018.
6. Hwang, H., S. Bae, and C. Lee, "Analysis and design of a hybrid rare-earth-free permanent magnet reluctance machine by frozen permeability method," *IEEE Trans. Magn.*, Vol. 52, No. 7, 1–4, 2016.
7. Hua, W., H. Zhang, M. Cheng, et al., "An outer-rotor flux-switching permanent-magnet-machine with wedge-shaped magnets for in-wheel light traction," *IEEE Trans. Ind. Electro.*, Vol. 64, No. 1, 3791–3799, Jan. 2017.

8. Hua, H., Z. Q. Zhu, C. Wang, et al., "Partitioned stator machines with NdFeB and ferrite magnets," *IEEE Trans. Ind. Appl.*, Vol. 53, No. 3, 1870–1882, 2017.
9. Awah, C. C., Z. Q. Zhu, Z. Z. Wu, H. L. Zhan, et al., "Comparison of partitioned stator switched slux permanent magnet machines having single- or double-layer windings," *IEEE Trans. Magn.*, Vol. 52, No. 1, 1–10, 2016.
10. Zhu, X., Z. Xiang, L. Quan, W. Wu, and Y. Du, "Multi-Mode optimization design methodology for a flux-controllable stator permanent magnet memory motor considering driving cycles," *IEEE Trans. Ind. Electron.*, Vol. 65 No. 7, 5353–5366, Jul. 2018.
11. Li, X., L. Quan, Y. Chen, et al., "Electromagnetic performance analysis of a new hybrid excited stator-partitioned flux switching permanent magnet machine," *2016 19th International Conference on Electrical Machines and Systems (ICEMS)*, 2016.
12. Sayed, E., Y. Yang, and B. Bilgina, "Comprehensive review of flux barriers in interior permanent magnet synchronous machines," *IEEE Access*, Vol. 7, 149168–149181, 2019.
13. Du, Y., W. Lu, X. Zhu, et al., "Optimal design and analysis of partitioned stator hybrid excitation doubly salient machine," *IEEE Access*, Vol. 6, 57700–57707, 2018.
14. Chen, M., K. T. Chau, C. H. T. Lee, and C. Liu, "Design and analysis of a new axial-field magnetic variable gear using pole-changing permanent magnets," *Progress In Electromagnetics Research*, Vol. 153, 23–32, 2015.
15. Zhu, X., D. Fan, Z. Xiang, et al., "Systematic multi-level optimization design and dynamic control of less-rare-earth hybrid permanent magnet motor for all-climatic electric vehicles," *Applied Energy*, DOI: 10.1016/j.apenergy.2019.113549.
16. Solmaz, K., G. Ali, M. Amin, A. R. Nasrudin, H. W. Ping, and N. Ud Mohammad, "Design optimization and analysis of AFPM synchronous machine incorporation power density, thermal analysis, and back-EMF THD," *Progress In Electromagnetics Research*, Vol. 136, 327–367, 2013.
17. Sun, X., L. Chen, H. Jiang, et al., "High-performance control for a bearingless permanent-magnet synchronous motor using neural network inverse scheme plus internal model controllers," *IEEE Trans. Ind. Electro.*, Vol. 63, No. 6, 3479–3488, 2016.
18. Edhah1, S. O., J. Y. AlSawalhi, and A. A. AlDurra, "Multi-Objective optimization design of fractional slot concentrated winding permanent magnet synchronous machines," *IEEE Access*, DOI: 10.1109/ACCESS.2019.2951023.
19. Du, G., W. Xu,. J. Zhu, et al., "Rotor stress analysis for high speed permanent magnet machines considering assembly gap and temperature gradient," *IEEE Transactions on Energy Conversion*, 2019. DOI: 10.1109/TEC.2019.2939220.
20. Zhu, X., M. Jiang, Z. Xiang, L. Quan, W. Hua, and M. Cheng, "Design and optimization of a flux-modulated permanent magnet motor based on an airgap-harmonic-orientated design methodology," *IEEE Trans. Ind. Electron.*, DOI: 10.1109/TIE.2019.2934063.
21. Zhu, X., W. Wu, L. Quan, Z. Xiang, and W. Gu, "Design and multi-mbjective stratified optimization of a less-rare-earth hybrid permanent magnets motor with high torque density and low cost," *IEEE Transactions on Energy Conversion*, Vol. 34, No. 3, 1178–1189, Dec. 2019.
22. Lei, G., C. Liu, J. Zhu, and Y. Guo, "Techniques for multilevel design optimization of permanent magnet motors," *IEEE Transactions on Energy Conversion*, Vol. 30, No. 4, 1574–1584, Dec. 2015.
23. Zhu, X., J. Huang, L. Quan, Z. Xiang, and B. Shi, "Comprehensive sensitivity analysis and multi-objective optimization research of permanent magnet flux-intensifying motors," *IEEE Trans. Ind. Electron.*, Vol. 66, No. 4, 2613–2627, Article No: 0602704, Apr. 2019.
24. Almandoz, G., I. Gómez, G. Ugalde, et al., "Study of demagnetization risk in PM machines," *IEEE Trans. Ind. Appli.*, DOI: 10.1109/TIA.2019.2904459, 2019.
25. Chen, L. L., C. S. Zhu, Z. X. Zhong, et al., "Rotor strength analysis for high-speed segmented surface-mounted permanent magnet synchronous machines," *IET Electric Power Applications*, Vol. 12, No. 7, 979–990, Jul. 2018.